

Identification of the wind in Rayleigh–Bénard convection

M. van Reeuwijk, H. J. J. Jonker, and K. Hanjalić

*Department of Multi-Scale Physics and J. M. Burgers Center for Fluid Dynamics,
Delft University of Technology, Lorentzweg 1, 2628 CJ Delft, The Netherlands*

(Received 17 January 2005; accepted 8 March 2005; published online 9 May 2005)

Using a symmetry-accounting ensemble-averaging method, we have identified the wind in unbounded Rayleigh–Bénard convection. This makes it possible to distinguish the wind from fluctuations and to identify dynamic features of each. We present some results from processing five independent three-dimensional direct numerical simulations of a $\Gamma=4$ aspect-ratio domain with periodic side boundaries at $Ra=10^7$ and $Pr=1$. It is found that the wind boundary layer scales linearly very close to the wall and has a logarithmic region further away. Despite the still noticeable molecular effects, the identification of log scaling and significant velocity and temperature fluctuations well within the thermal boundary layer clearly indicate that the boundary layer cannot be classified as laminar. © 2005 American Institute of Physics.

[DOI: 10.1063/1.1920350]

Recent theories for the prediction of the scaling behavior of the nondimensional heat flux Nu and the Reynolds number Re in the Rayleigh–Bénard convection presume the existence of “wind,”^{1,2} a large scale circulation that autonomously arises in the system. Indeed, this circulation has been observed by various groups and received quite some attention over the last years.^{3–9} The theories use wind primarily as a conceptual notion; little is known about the actual magnitude of the wind as compared to velocity fluctuations and if it is present for all Rayleigh numbers.⁹ But most important, a straightforward definition of wind seems to be missing. The natural candidates are the ensemble average, a time average over a sufficiently long period, a spatial average over a sufficiently large area, and a combination of the three. However, the problem is that all these averages yield a vanishing wind $\bar{u}=0$. For the ensemble average and the spatial average this may be obvious from symmetry considerations (see below), but for the time average it is more subtle. In this context the experiments^{5,9} are most instructive. Here it is shown that the wind erratically reverses its direction on time scales far exceeding the convective turnover time, Sreenivasan, Bershadskii, and Niemela⁹ propose a simple dynamical picture to explain these wind reversals, with two metastable states, i.e., clockwise and counterclockwise mean wind motions; only extreme events, such as (a combination of) energetic plumes, can flip the system from one state to another. The relevant point here is that the reversals actually conserve the *ergodicity* of the system: the (long) time average becomes equal to the ensemble average—which is zero. The purpose of this letter is therefore to come up with a suitable and useful definition of wind. Based on this definition we then determine the wind based on five direct numerical simulations (DNS) of moderate aspect ratio and with periodic side boundaries. An analysis of the wind field and fluctuations shows evidence of a boundary layer that is not laminar.

The Rayleigh–Bénard convection is generated when a layer of fluid with thickness H is subjected to a positive temperature difference Δ between the bottom and top wall.

Within the Boussinesq approximation, the only control parameters are the Rayleigh number $Ra=\beta g\Delta H^3(\nu\kappa)^{-1}$ and the Prandtl number $Pr=\nu/\kappa$. Here ν is the kinematic viscosity, κ is the thermal diffusivity, and β is the expansion coefficient. In domains with finite size, the aspect ratio $\Gamma=L/H$, with L as the horizontal extent of the layer, is an additional control parameter. The direction of gravity pointing in the negative z direction, the equations for momentum, continuity, and heat transfer are given by

$$\partial_i u_i + u_j \partial_j u_i + \rho^{-1} \partial_i p - \nu \partial_j^2 u_i = \beta g \Theta \delta_{i3}, \quad (1)$$

$$\partial_j u_j = 0, \quad (2)$$

$$\partial_i \Theta + u_j \partial_j \Theta - \kappa \partial_j^2 \Theta = 0, \quad (3)$$

with ρ as the density, u_i as the velocity, Θ as the temperature, and p as the pressure.

Since definitions for the processes occurring in the Rayleigh–Bénard convection are not unambiguously defined, a small glossary is given here. We prefer to use the term *convective structure*, which generalizes the terms wind and large-scale circulation, in that it involves both the velocity and the temperature field. This convective structure normally features convection rolls, which are the steady roll-like structures. Plumes are the unsteady structures erupting from the boundary layers and propagating to the other side. Spatial averages will be denoted by $\langle \rangle_A$ and $\langle \rangle_H$ for plane and height averaging, respectively.

Invariant to translation and rotation, Eqs. (1)–(3) contain many symmetries, e.g.^{10,11} The domain and boundary conditions put additional constraints on the symmetries but for sufficiently simple domains, many symmetries remain. In the solutions of (1)–(3), a subset of these symmetries will show up, although—due to the nonlinear interactions—for large Rayleigh numbers only in an average sense.¹⁰

Instead of $u_i=0$ being the trivial solution, one may have an image in which the zero ensemble mean consists of groups of superimposed equiprobable conjugate symmetrical

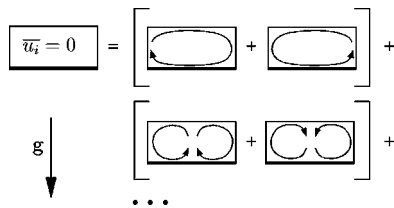


FIG. 1. Convection cell with zero mean flow. The zero ensemble mean solution is the result of a superposition of conjugate symmetric modes.

modes, as shown in Fig. 1. Here a two-dimensional cell is sketched, together with some possible convective structures (modes). Focusing on the situation with one roll, the clockwise and counterclockwise modes are qualitatively and after a reflective operation also quantitatively identical. A more thorough and precise treatment of these arguments can be found in Refs. 11 and 12.

Thus although mathematically correct, the ensemble mean $\bar{u}_i=0$ does not necessarily represent a physical mode of the system. Therefore, we argue that for a useful interpretation of results it is important to account for these symmetries and present a generalized ensemble-averaging method that is able to do so. In classical ensemble averaging the average is defined as $\bar{X} \equiv 1/N \sum_{\alpha=1}^N X^{(\alpha)}$ with N as the number of realizations and $X=X(\mathbf{x})$. To extend this to a symmetry-accounting ensemble-averaging method, we have to apply some operations before averaging:

$$\tilde{X} \equiv \frac{1}{N} \sum_{\alpha=1}^N S^{(\alpha)} X^{(\alpha)}. \quad (4)$$

Here $S^{(\alpha)}$ is an operator S for realization α . The operator S is composed of one or more elementary symmetry operators $S^{(\alpha)}=S_1 \circ S_2 \circ \dots$, such as horizontal or vertical reflections. The elementary operators follow directly from the symmetries of the domain and boundary conditions. Classical ensemble averaging now reduces to the case when S is the identity. Like in classical ensemble averaging, we can decompose the fields in a symmetry-accounted mean and fluctuating part as $X=\tilde{X}+X'$.

Applying these concepts to our problem with periodic sidewalls, the most important symmetry that must be accounted for is the translation invariance in x, y . This operation is denoted by S_r with $\mathbf{r} \equiv (r_x, r_y)$ as the relative displacement. This would make the displacement \mathbf{r} the only unknown per realization, but unfortunately the convective structure is not known either *a priori*, which we address by using an iterative pattern-recognition technique.¹³ With this technique the convective structure and the displacements are determined simultaneously, gradually improving the estimation for the convective structure in successive iterations. The only assumption needed for this method is that—among all realizations—one and only one persistent structure (mode) is present inside the domain.

To start the iterative pattern-recognition process a reference field $X_0(\mathbf{x})$ is needed, for which a randomly picked realization is used—the convective structure is present in every realization so the starting point should not make a differ-

ence. Using a correlation function $C(X, Y)$, every realization can be compared to $X_0(\mathbf{x})$, and the location of maximum correlation is picked as the displacement vector,

$$\mathbf{d}^{(\alpha)} \leftarrow \max_{\mathbf{r}} C(S_r X^{(\alpha)}, X_0). \quad (5)$$

There is some freedom in choosing how to calculate the overall two-dimensional (2D) correlation field, as it is constructed from $X \in \{u_i, \Theta, p\}$. In this case we opted for the instantaneous height-averaged temperature $\langle \Theta \rangle_H$ which is closely related to the convective structure as $\langle \Theta \rangle_H > 0$ where $w > 0$ and vice versa. After calculating $\mathbf{d}^{(\alpha)}$ for all realizations and using (4), a new and improved estimation can be determined by

$$\tilde{X}_{n+1} = \frac{1}{N} \sum_{\alpha=1}^N S_{\mathbf{d}^{(\alpha)}} X^{(\alpha)}. \quad (6)$$

Repeatedly applying (5) with X_0 replaced with X_n and (6) until $\tilde{X}_{n+1}(\mathbf{x}) = \tilde{X}_n(\mathbf{x}) = \tilde{X}(\mathbf{x})$ results in the convective structure, or symmetry-accounted average (4), as well as the relative displacements $\mathbf{d}^{(\alpha)}$.

The DNS used for this analysis integrates Eqs. (1)–(3) with a second-order Adams–Bashforth time-marching algorithm. The grid is equidistant, staggered and all derivatives are discretized with central differences. The boundary conditions are periodic for the side boundaries; the top and bottom walls have no-slip velocity and fixed temperature. The simulations reported here are done at $Ra=1 \times 10^7$, $Pr=1$, and with an aspect-ratio $\Gamma=4$ domain, the grid consisting of 256^3 cells. For this Ra , the convective turnover time based on the maximum variance of horizontal velocity is $t^*=40$ s; the nondimensional time is defined as $\hat{t} \equiv t/t^*$. In total five independent simulations have been performed.

Figure 2 shows four successive time shots of one of the simulations for the height-averaged temperature $\langle \Theta \rangle_H$, which clearly show the persistence of the convective structure and its growth in time. At $\hat{t}=12.5$ [Fig. 2(a)], the flow is organized into two up- and downward regions, then follows an intermediate situation [Fig. 2(b)], resulting in a configuration with one up- and downward region [Figs. 2(c) and 2(d)]. The growth of convective structures has been observed before,^{6,14,15} and goes on long after the process is statistically stationary. Although the details of the field are very unsteady as plumes rise and fall, the large-scale pattern is remarkably steady as Figs. 2(c) and 2(d) clearly show, indicating the presence of a persistent convective structure.

Applying symmetry-accounting ensemble averaging on about 200 independent realizations, Fig. 3 shows the average wind field (convective structure). The realizations are taken from five independent simulations at intervals of $\Delta \hat{t}=0.5$, from the moment the flow has developed to its largest scale. In the lower boundary layer, the streamlines [Fig. 3(a)] clearly show an attracting region where the flow is upward; one repelling region where the flow is downward and two saddle points. The height-averaged temperature $\langle \tilde{\Theta} \rangle_H$ [Fig. 3(a)] is consistent with this picture, as the relatively hot fluid is carried upwards and vice versa. Figure 3(b) shows a side view of the average field after averaging over the y direction.

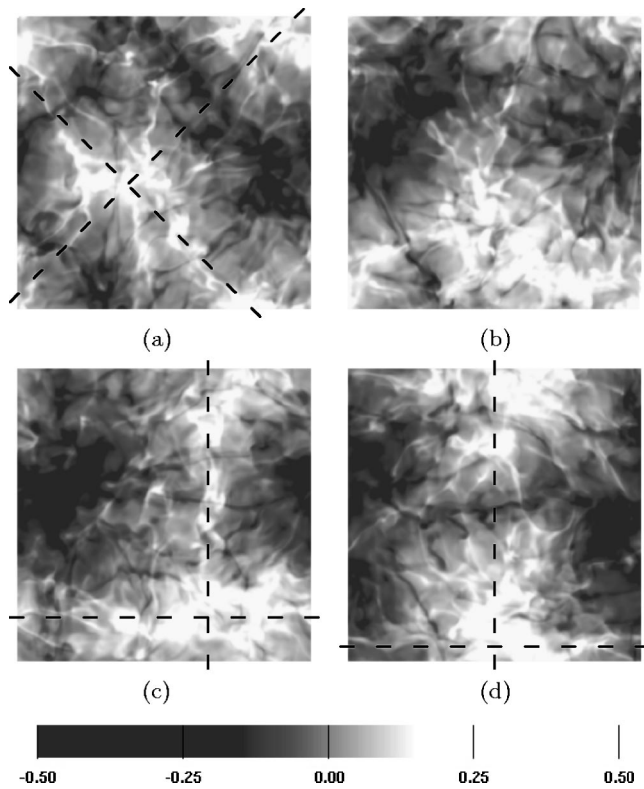


FIG. 2. Development and growth of large-scale structures in time as indicated by the instantaneous height-averaged temperature $\langle \Theta \rangle_H$. (a) $\hat{t} = 12.5$; (b) $\hat{t} = 16.75$; (c) $\hat{t} = 22.25$; (d) $\hat{t} = 37.5$.

The contour lines are of relative temperature, which is the deviation from the plane-averaged temperature $\langle \tilde{\Theta} \rangle_A(z)$. Clearly visible in the figure is the projection of the two rolls onto the side view. This result may clarify why two-dimensional simulations are able to predict the $Ra-Re-Nu$ behavior reasonably well.¹⁶

Decomposed in a contribution due to the convective structure $\tilde{u}_i \tilde{u}_i$ and to plumes and turbulence $u'_i u'_i$, the plane-averaged distribution of kinetic energy along the vertical is an indication for the magnitude of wind and fluctuations. The total kinetic energy k is given by $k = (\langle \tilde{u}_j \tilde{u}_j \rangle_A + \langle u'_j u'_j \rangle_A) / 2$ and it can be seen [Fig. 3(c)] that the energy contained in the vertical fluctuations $\langle w' w' \rangle_A$ is higher than in the convective structure $\langle \tilde{w} \tilde{w} \rangle_A$, indicating that the instability-generated plumes dominate in the vertical transport. In the horizontal, the average and fluctuating parts are of similar magnitude, with a striking difference that the squared mean horizontal velocity $\langle \tilde{u} \tilde{u} \rangle_A$ peaks at the hydrodynamic boundary layer, but the mean squared velocity $\langle u' u' \rangle_A$ is quite uniformly distributed outside the boundary layers, revealing a well-mixed bulk. Here we distinguish a thermal boundary layer λ_Θ , defined as the location of maximum temperature variance $\langle \Theta' \Theta' \rangle_A$ and a hydrodynamic boundary layer λ_u , defined by the location of maximum squared mean horizontal velocity $\langle \tilde{u} \tilde{u} \rangle_A$. It can be appreciated that even deep inside the thermal boundary layer λ_Θ [inset Fig. 3(c)], the mean squared horizontal velocity $\langle u' u' \rangle_A$ is significant and of the same order as the squared mean velocity $\langle \tilde{u} \tilde{u} \rangle_A$.

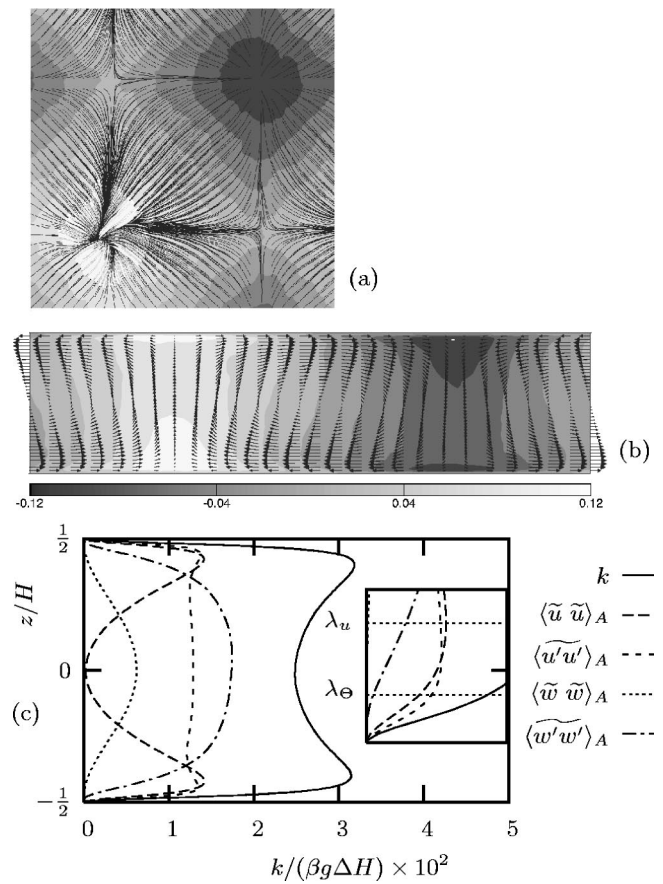


FIG. 3. Symmetry-accounted wind field; (a) streamlines at the edge of bottom thermal boundary layer with contours of height-averaged temperature $\langle \tilde{\Theta} \rangle_H$; (b) the wind field averaged over the y direction [top to bottom in Fig. 3(a)]; (c) distribution of kinetic energy and along the vertical, decomposed in symmetry-accounted average and fluctuation components; inset: close-up of the boundary layer.

Focusing on the hydrodynamic boundary layer, the inset of Fig. 4(a) shows the horizontal velocity profile nondimensionalized with the wall-shear stress, where $u^+ \equiv u/u_*$, $z^+ \equiv z u_* / \nu$, with the friction velocity $u_* \equiv \sqrt{\tau_s / \rho}$ and local wall-shear stress τ_s . The velocity profiles are obtained by taking equidistant vertical cuts from the average field shown in Fig. 3(b). Clearly, scaling with the wall-shear stress does not yield a universal profile, indicating that the effects of buoyancy are not negligible—as would be expected from a buoyancy-driven flow. However, all profiles do collapse upon normalization of z by the local hydrodynamic boundary layer thickness $\lambda_u(x)$ and u by the wind maximum $u_\lambda(x) = u(x, \lambda_u(x))$ [Fig. 4(a)]. The universal profile shows a linear near-wall profile [Fig. 4(b)], followed by a short region with logarithmic scaling [Fig. 4(c)].

According to the classic similarity theory for forced convection, the existence of a logarithmic behavior indicates the presence and dominance of turbulence. However, Fig. 4(c) shows that the logarithmic region starts well inside the thermal boundary layer where the molecular effects are not negligible. On the other hand, from the profiles of components of kinetic energy it is clear that the horizontal fluctuations $\langle u' u' \rangle_A$ are significant deep inside the thermal boundary

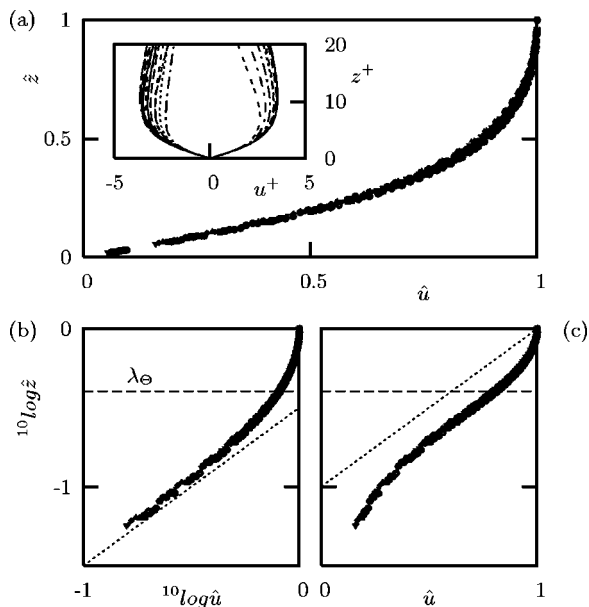


FIG. 4. Horizontal velocity profile in boundary layer: (a) normalized as $\hat{u} = \bar{u}/\bar{u}_\lambda$ and $\hat{z} = z/\lambda_u$ with $u_\lambda(x) = u(x, \lambda_u(x))$. Inset: nondimensionalized with wall-shear stress. (b) Log-log plot of \hat{u} , showing a linear near-wall profile. (c) Semilog plot of \hat{u} , showing a logarithmic region.

layer, showing that the boundary layer is not laminar. Perhaps the action of plumes, major contributors to the fluctuations, cause the boundary layer's dual behavior—an idea that Kerr¹⁷ also adopts after an analysis of dissipation rates. Whether the velocity fluctuations $\langle u'u' \rangle_A$ have true features of turbulence can be judged only after a thorough analysis of the spectrum and other turbulence indicators, which is beyond the scope of this letter.

This work is supported by the Stichting voor Fundamenteel Onderzoek der Materie (FOM). The computations were sponsored by the National Computing Facilities Foundation (NCF) for the use of supercomputing facilities, with financial support from the Nederlandse Organisatie voor Wetenschappelijk Onderzoek (NWO).

- ¹S. Grossmann and D. Lohse, "Scaling in thermal convection: a unifying theory," *J. Fluid Mech.* **407**, 27 (2000).
- ²B. I. Shraiman and E. D. Siggia, "Heat transport in high Rayleigh-number convection," *Phys. Rev. A* **42**, 3650 (1990).
- ³B. Castaing *et al.*, "Scaling of hard thermal turbulence in Rayleigh-Bénard convection," *J. Fluid Mech.* **204**, 1 (1989).
- ⁴R. Krishnamurti and L. N. Howard, "Large-scale flow generation in turbulent convection," *Proc. Natl. Acad. Sci. U.S.A.* **78**, 1981 (1981).
- ⁵J. J. Niemela, L. Skrbek, K. R. Sreenivasan, and R. J. Donnelly, "The wind in confined thermal convection," *J. Fluid Mech.* **449**, 169 (2001).
- ⁶A. Parodi *et al.*, "Clustering of plumes in turbulent convection," *Phys. Rev. Lett.* **92**, 194503 (2004).
- ⁷X.-L. Qiu and P. Tong, "Large-scale velocity structures in turbulent thermal convection," *Phys. Rev. E* **64**, 036304 (2001).
- ⁸E. B. Siggia, "High Rayleigh number convection," *Annu. Rev. Fluid Mech.* **26**, 136 (1994).
- ⁹K. R. Sreenivasan, A. Bershadskii, and J. J. Niemela, "Mean wind and its reversal in thermal convection," *Phys. Rev. E* **65**, 056306 (2002).
- ¹⁰U. Frisch, *Turbulence* (Cambridge University Press, Cambridge, 1995).
- ¹¹M. Golubitsky and I. Stewart, *The Symmetry Perspective* (Birkhauser, Basel, 2002).
- ¹²P. Chossat and M. Golubitsky, "Symmetry-increasing bifurcation of chaotic attractors," *Physica D* **32**, 423 (1988).
- ¹³O. S. Eiff and J. F. Keffer, "On the structures in the near-wake region of an elevated turbulent jet in a crossflow," *J. Fluid Mech.* **333**, 161 (1997).
- ¹⁴S. R. de Roode, P. G. Duynkerke, and H. J. J. Jonker, "Large-eddy simulation: How large is large enough?" *J. Atmos. Sci.* **61**, 403 (2004).
- ¹⁵T. Hartlep, A. Tilgner, and F. H. Busse, "Large scale structures in Rayleigh-Bénard convection at high Rayleigh numbers," *Phys. Rev. Lett.* **91**, 064501 (2003).
- ¹⁶S. Kenjereš and K. Hanjalić, "Numerical insight into flow structure in ultraturbulent thermal convection," *Phys. Rev. E* **62**, 7987 (2000).
- ¹⁷R. M. Kerr, "Energy budget in Rayleigh-Bénard convection," *Phys. Rev. Lett.* **87**, 244502 (2001).